Ocean Engineering 320 (2025) 120189

Contents lists available at ScienceDirect

Ocean Engineering

journal homepage: www.elsevier.com/locate/oceaneng

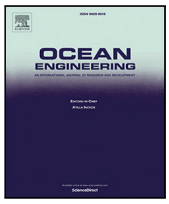

Research paper

Full-scale experimental research on wave shielding effect of RV Gunnerus for offshore operations

Tongtong Wang *, Robert Skulstad, Finn Tore Holmeset, Karl Henning Halse, Hans Petter Hildre, Houxiang Zhang

Department of Ocean Operations and Civil Engineering, Norwegian University of Science and Technology (NTNU), 6009 Aalesund, Norway

ARTICLE INFO

Keywords:
Shield effect
Field experiment
Offshore vessel
Short-crested waves
Crane operations

ABSTRACT

The investigation of wave shielding effects holds significant importance for practical offshore operations. Utilizing the calm area on the lee side of the vessel enables operations to enhance safety and efficiency. Optimized vessel heading control reduces the relative motions in crane operations, thereby increasing the operational window. To achieve this, we conducted full-scale field experiment research with the research vessel Gunnerus, delivering more reliable and credible results to bridge the gap from simulations to real-world conditions. A detailed examination of experimental data and analysis reveals that when the ship encounters two short-crested waves with nearly 90° directional difference, the largest crane motion and optimal shelter effects occur when the vessel is beam-on to the stronger wave. Crane motion was more sensitive to wave attack angles than to the amplitude of the shielded wave. Specifically, positioning the vessel between 165° and 180° relative to the stronger wave minimized wave elevation in the sheltered zone and reduced vertical crane movements. Additionally, headings between 90° and 120° created a sufficiently calm area for efficient operations. These insights provide practical implications for optimizing vessel positioning and enhancing operational efficiency in challenging marine environments.

1. Introduction

The digital transformation and distributed technologies change the maritime business (Zhang et al., 2023). By leveraging tools such as big data analytics, automation, and the Internet of Things (IoT), modern maritime operations can optimize routes, monitor vessel performance (Wang et al., 2021), and improve decision-making processes (Wang et al., 2022). Despite the growing focus on maritime autonomous surface ships (MASS), these technologies remain in their early stages (Chang et al., 2021), and their full potential can only be realized through rigorous testing under real-world conditions. Simulation or scaled laboratory tests are insufficient in replicating the complexities of physical and environmental forces faced during maritime operations, making field experiments vital.

Fjordlab Å lesund addresses the requirement for a full-scale field laboratory for research on the development of marine technology and science. It is a developing laboratory for full-scale testing of ships, ship equipment, navigation, autonomy, coastal traffic, and technology for monitoring the ocean and vulnerable coastal infrastructure. It includes harsh open sea conditions, sheltered-, shallow- and deep-sea environmental conditions. Among the various challenges encountered in maritime operations, wave impacts present significant risks. Understanding and developing effective wave shielding techniques, where structures or methods are used to reduce wave impacts, can enhance the resilience of vessels and offshore platforms. This is especially important as maritime activities expand into deeper waters, where wave hazards become more frequent.

Ensuring safety in offshore operations, such as during maintenance activities, depends heavily on mitigating relative motions between vessels (Ren et al., 2021). For instance, when accommodation vessels that provide offshore maintenance, crew transfer, and catering-related support are connected side-to-side by the gangway to an FPSO (Floating Production Storage and Offloading) platform, large strokes of the gangway should be avoided to improve its lifespan (Cong et al., 2018; Li, 2021). Similar challenges arise in the installation of offshore wind turbines (Li et al., 2015; Guanche et al., 2016), where relative motion between floating units can lead to dangerous forces on connecting equipment, such as high tension of connecting hawser, high compressing of fenders, and even collision between hulls. Therefore, consideration should be given to canceling the relative motion between bodies, bringing higher working limits.

* Corresponding author.
E-mail addresses: tongtong.wang@ntnu.no (T. Wang), robert.skulstad@ntnu.no (R. Skulstad), fiho@ntnu.no (F.T. Holmeset), karl.h.halse@ntnu.no (K.H. Halse), hans.p.hildre@ntnu.no (H.P. Hildre), hozh@ntnu.no (H. Zhang).

https://doi.org/10.1016/j.oceaneng.2024.120189
Received 19 September 2024; Received in revised form 24 October 2024; Accepted 20 December 2024
Available online 8 January 2025

Through literature review, it is found that the hydrodynamic interactions among multiple bodies may raise concerns that threaten safety and operability, particularly when resonance effects amplify the dynamic response. Studies such as (Zhao et al., 2018) have investigated these phenomena, revealing the importance of managing vessel positions and mitigating motions during side-by-side configuration. Li (2020) modeled the multi-body dynamics effects and analyzed the resonant characteristics of parallel and nonparallel configurations. Oh et al. (2020) found that vessels positioned in the shelter of larger structures can experience a reduced dynamic response. Huang et al. (2023) looked into the dynamic response of floating bridges with a floating platform constructed on the waterside and found that due to the shielding effect of the floating platform, the motions in heave, surge, and pitch of the floating bridge are evidently diminished. Li et al. (2016) analyzed the lifting operation of a monopile of an offshore wind turbine in a shielding area in short-crested waves, and found that the monopile responses are consequently reduced. Cong et al. (2018) considered a floatel working in the vicinity of the FPSO platform side-by-side connected by a telescoping personnel gangway. Upon hydrodynamic analysis, a controller was designed to avoid large strokes of the gangway with the shielding effect accounted for. Furthermore, it is found that during offloading, the power demand from the dynamic position (DP) system to maintain constant positions with the FPSO for a shuttle tanker is reduced because of the shielding effects (Queiroz Filho and Tannuri, 2009). These findings make wave shielding a key factor in enhancing operational safety.

By strategically positioning vessels and utilizing wave shielding, operators can reduce vessel motions and improve the stability of operations, particularly in offshore environments where sea conditions are unpredictable. In theory, the wave surface motion in the shielded area depends on the wavelength, the size of the blocking body, and the wave direction. Research on wave shielding effects has been of interest for decades, but most of them are conducted numerically. Due to the facility complexity and economic cost, the shielding effects and operation heading optimization are seldom investigated experimentally, especially on a full scale. In this paper, attention is focused on the possibility of placing the vessel and lifting system in a good position to minimize the relative motion and increase the operational weather window benefiting from the shielding effects. The research vessel Gunnerus with crane is positioned at different wave headings in the open sea, aiming to block waves. A light crane lift where the weight of the structure does not affect the motion characteristics of the vessel is considered. The vessel shielding effects are investigated through a detailed examination of experimental data and analysis under different wave headings. By elucidating the mechanisms and practical implications of vessel shielding, we aim to bridge the gap between simulation and practical marine lifting operations, providing valuable pragmatic insights to enhance the safety, efficiency, and sustainability of offshore operations.

The remainder of this paper is organized as follows: Section 2 introduces the experiment setup, including the device deployment and data collection mechanisms. Section 3 presents the experiment performance of the surface vessel, as well as the wave elevations in the sheltered area. Time-series analysis and frequency domain analysis of the relative motion between the crane and underneath waves are conducted. The experimental results are discussed in Section 4. Section 5 concludes the paper and summarizes the key findings.

2. Experiments setup

2.1. Deployment

The experimental setup consists of the vessel RV Gunnerus,[1] the vessel's data-logging system, the vessel's crane, and one wave buoy. The research vessel (RV) Gunnerus, owned and operated by the Norwegian University of Science and Technology, is utilized as the floating platform to block waves. The RV Gunnerus is equipped with two permanent magnet-driven azimuth thrusters at the stern and one tunnel thruster at the bow. The data acquisition system onboard collects data through various channels, covering ship motion, crane, and ocean environments,[2] as summarized in Table 1. The Palfinger crane is installed at the starboard, with a three-dimensional accelerometer additionally attached to the hook to measure the tip motion. The main dimensions of the vessel and crane are presented in Table 2.

Table 1
Data channels sensed onboard the R/V Gunnerus.

	Signal	Channels	Unit
Vessel	GNSS	Latitude	ddmm.mmmm
		Longitude	ddmm.mmmm
		Course angle	deg
		Speed over ground	knots
	MRU	Heading angle	deg
		Heading rate	deg/s
		Roll angle	deg
		Pitch angle	deg
		Heave displacement	m
		Roll rate	deg/s
		Pitch rate	deg/s
		Heave rate	m/s
	Wind sensor	Wind direction	deg
		Wind speed	knots
	Wave radar	Directional wave spectrum	m^2/Hz
	Rangefinder	Air gap	m
Crane	Operation	Slewing angle	deg
		Outer boom angle	deg
		Main boom angle	deg
		Extension length	m
	End-effector	Three-dimensional accelerometer	m/s^2

During the experiment, the vessel was dynamically positioned. The wave buoy was deployed at the starboard side of the vessel to detect the wave elevations in the sheltered areas. The buoy was attached to a floating device with a 3.5-meter-long rope, as shown in Fig. 1(a). 1.25 meters from the buoy, there was a weight of approx. 775 grams. This floating device was secured through the crane hook so it could be deployed from the ship's deck and adjusted aside from the ship, as indicated in Fig. 1(b). The crane was then positioned 90° out of the starboard side of the vessel, with the boom tip in a horizontal position. This position is considered the normal place to deploy equipment from the vessel's deck with the crane. The layout of the crane and wave buoy was deployed as Fig. 2(a).

In general, sea states are composed of various wave types, including swell and wind waves. Wind sea waves are generated by local winds, while swell waves originate from strong winds in distant areas (Semedo et al., 2015). These different waves often come from different directions and have varying periods. In the experiment, the vessel was initially positioned with its bow facing the local wind. The heading was then adjusted every 15 min, gradually exposing the vessel to wind coming from the beam, as shown in Fig. 2(b). The ship heading changes by 15° in every scenario. The crane is kept still during course changes; thereby, the horizontal relative positions between the crane and buoy are maintained.

2.2. Ship crane lifting

The crane generally does not have any fixed sensor for measuring the crane-tips movement. The movement of the crane tip, which is

[1] https://www.ntnu.edu/gunnerus

[2] The wave radar and rangefinder used in this experiment: https://www.miros-group.com/

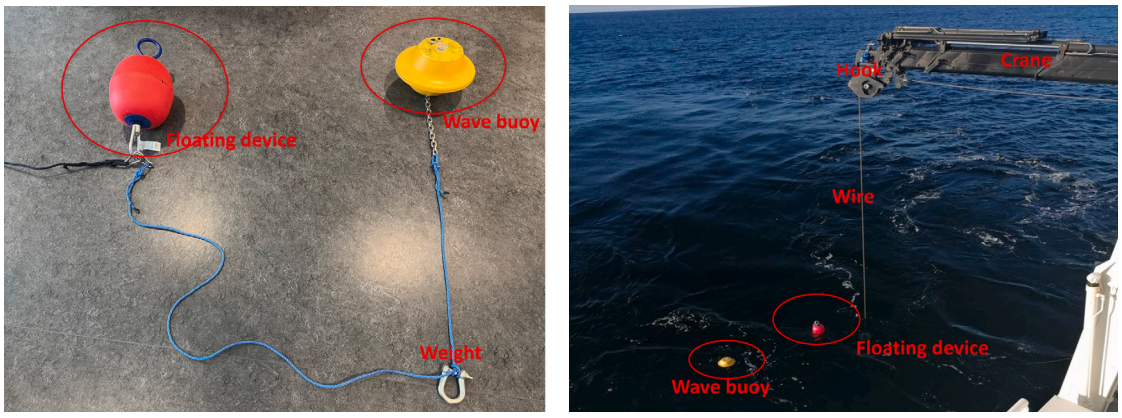

(a) (b)

Fig. 1. Experimental device layout.

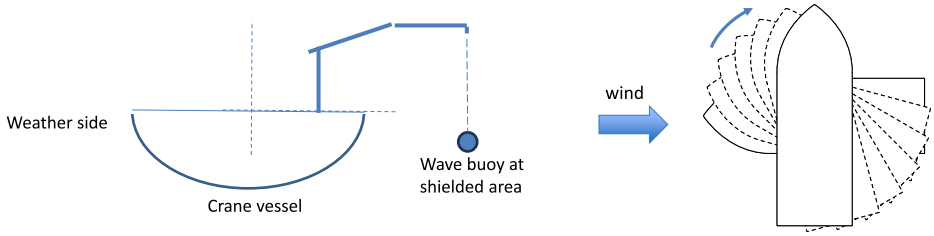

(a) Device layout. (b) Ship heading changes.

Fig. 2. Experiment setup.

Table 2
Main dimensions of the research vessel and crane.

	Parameters	Value
Vessel	Length overall (L_{oa})	36.25 m
	Length between perpendicular (L_{pp})	33.9 m
	Waterline length (L_{wl})	29.9 m
	Breadth middle (B_m)	9.6 m
	Breadth extreme (B)	9.9 m
	Depth mld. Min deck (Dm)	4.2 m
	Draught, mld (dm)	2.7 m
	Displacement	543.79 t
Crane	Max.lifting moment	62 mt
	Max.lifting capacity	22 t
	Max.hydraulic outreach	20.4 m
	Slewing torque with one gear	4.5 mt
	Stabilizer spread (std)	8.6 m
	Max.operating pressure	365 bar
	Deadweight	5040 kg

also named the end-effector, is transmitted through the ship response. To begin with, the crane is assumed to have a rigid connection with the ship hull, and the hook virtually suspends the lightweight payload without winch payout, so the motion of the payload identifies that of the crane tip.

The analysis of the ship-crane system is presented. The motion transformation is implemented through the forward kinematics. Fig. 3(a) displays the Palfinger crane onboard the vessel, and the kinematic references from the foundation to the tip are organized as Fig. 3(b). The crane tip Cartesian positions relative to the crane foundation are derived through the Denavit–Hartenberg (D–H) method (Craig, 2006). The D–H method gives a homogeneous transformation matrix ${}^{i-1}_{i}T$ from the reference frame i to reference frame $i-1$ (1).

$$ {}^{i-1}_{i}T = \begin{bmatrix} c\theta_i & -s\theta_i & 0 & a_{i-1} \\ s\theta_i c\alpha_{i-1} & c\theta_i c\alpha_{i-1} & -s\alpha_{i-1} & -s\alpha_{i-1} d_i \\ s\theta_i s\alpha_{i-1} & c\theta_i s\alpha_{i-1} & c\alpha_{i-1} & c\alpha_{i-1} d_i \\ 0 & 0 & 0 & 1 \end{bmatrix} \tag{1} $$

where

a_{i-1}: the offset distance from Z_{i-1} to Z_i along X_{i-1};
α_{i-1}: the offset angle from Z_{i-1} to Z_i about X_{i-1};
d_i: the distance from X_{i-1} to X_i along Z_i;
θ_i: joint angle from X_{i-1} to X_i about Z_i.
$c\cdot = \cos(\cdot), s\cdot = \sin(\cdot)$.

Through the forward kinematic transformation matrix, the crane tip Cartesian positions relative to the crane foundation are derived through:

$$ P_0 = {}^{0}_{1}T \cdot {}^{1}_{2}T \cdot {}^{2}_{3}T \cdot {}^{3}_{4}T \cdot {}^{4}_{5}T \cdot {}^{5} P = {}^{0}_{5}\mathrm{T} \cdot P \tag{2} $$

where P is the position vector in the end effector frame. The details of the transformation matrix can be referred to Chu et al. (2021).

Then, according to the crane base frame and the ship body frame shown in Fig. 3(c), the crane tip position in the crane base frame is then transferred to the ship body frame represented as P_{cg} that is oriented with the center of gravity of the vessel through translation and rotation matrix:

$$ P_{cg} = T_{translation} + RP_0 = \begin{bmatrix} \Delta x \\ \Delta y \\ \Delta z \end{bmatrix} + \begin{bmatrix} 0 & 1 & 0 \\ -1 & 0 & 0 \\ 0 & 0 & 1 \end{bmatrix} P_0 \tag{3} $$

At the end, the tip position represented in the global coordinates, i.e., the North-East-Down frame is presented as:

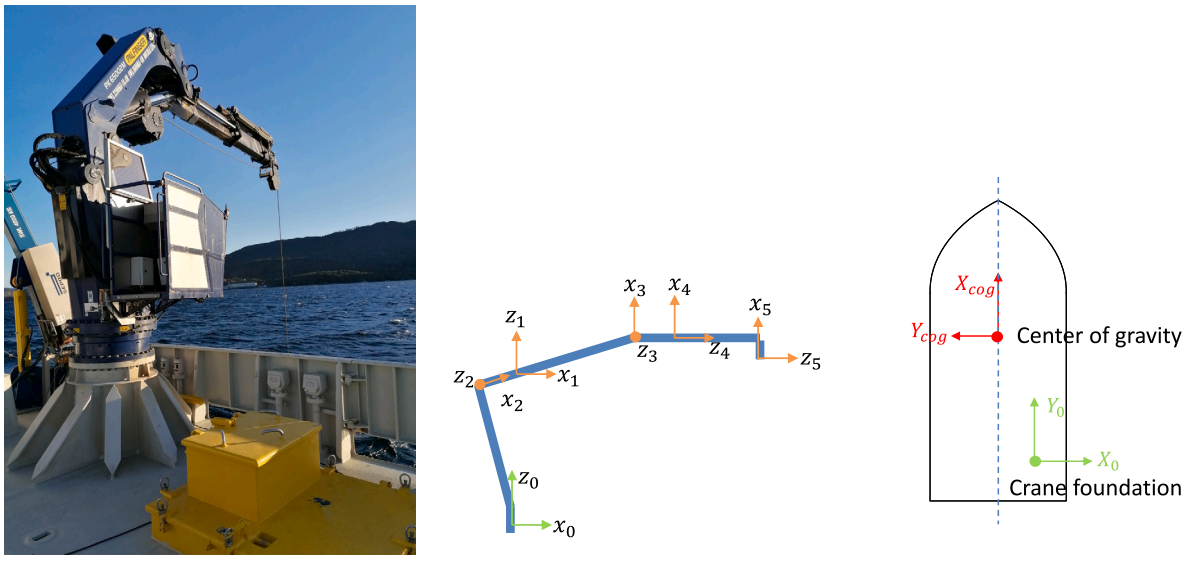

(a) (b) (c)

Fig. 3. (a) Palfinger crane installed onboard; (b) kinematic reference of the Palfinger crane from foundation to tip; (c) reference frame of the crane base in ship body frame and global frame.

$$P = \begin{bmatrix} x_{surge} \\ y_{sway} \\ z_{heave} \end{bmatrix} + \begin{bmatrix} \cos\psi\cos\theta & \cos\psi\sin\theta\sin\phi - \sin\psi\cos\phi & \cos\psi\sin\theta\cos\phi + \sin\psi\sin\phi \\ \sin\psi\cos\theta & \sin\psi\sin\theta\sin\phi + \cos\psi\cos\phi & \sin\psi\sin\theta\cos\phi - \cos\psi\sin\phi \\ -\sin\theta & \cos\theta\sin\phi & \cos\theta\cos\phi \end{bmatrix} P_{cg} \tag{4}$$

where ψ, θ, ϕ represents ship yaw, pitch, roll angles. Thus, the crane end-effector motion can be perceived as a function of ship 6 DoF movement and crane variables.

2.3. Floating buoy at the sheltered area

A small wave buoy with a diameter of 32 cm, a height of 22 cm, and a weight of 3.5 kg[3] was deployed as described in Section 2.1 to detect the wave elevations at the starboard side of the vessel. The buoy holds a Micro-ElectroMechanical-Systems (MEMS) device that contains a 3-axis accelerometer, a 3-axis gyroscope, and a 3-axis magnetometer. Through sensor fusion, this device outputs the three-dimensional acceleration and orientation at 50 Hz (Alari et al., 2022).

The wave measurements are based on the fact that the buoy will respond to the waves by following the height and slope of the waves so that the wave buoy motion can be interpreted as the motion of the sea surface. As the tilt angle leads to a change in the acceleration, the measured vertical acceleration is calibrated to an Earth reference frame based on the rotation principle:

$$z_c = z\cos\theta\cos\phi \tag{5}$$

where θ and ϕ are the pitch and roll angles of the buoy, respectively. z is the raw measured vertical acceleration, and z_c is the vertical acceleration after calibration. The wave surface elevation is obtained by double integrating the data from the inertial sensors, and wave parameters and spectrum are transmitted as well. The data processing follows the one used in Alari et al. (2022) with modifications to the specific dataset. In this experiment, each deployment takes 15 min. The 15-minute displacement time series is used to calculate wave spectra from a quarter signal blocks using the Welch method with 50% overlap. From the wave spectrum $S(\omega)$, the integrated wave parameters — significant wave height H_s and mean wave period T_m are evaluated as (6).

$$\begin{aligned} H_s &\approx 4\sqrt{m_0} \\ T_m &\approx m_{-1}/m_0 \end{aligned} \tag{6}$$

The spectral moment of order n is defined as:

$$m_n = \int \omega^n S(\omega) d\omega \tag{7}$$

3. Experiment results

The experiment took place on 30th October 2023, at Breisundet, Norway. The vessel RV Gunnerus was dynamically positioned at the location indicated in Fig. 4(a). Using the Miros wave radar, the directional wave spectrum was measured. The resulting $S(\omega, \theta)$ matrix, a discretized 36 × 32 array, provides data for 36 wave directions (10° intervals) and $N_\omega = 32$ wave frequencies ranging from 0 to 0.32 Hz with 0.01 Hz interval. A visualization of the wave spectrum is displayed in Fig. 5(a), where the North is up, indicating the energy distribution across wave frequencies and directions. Two energy clusters are evident, revealing the presence of two main wave systems with various magnitudes. The integrated spectrum Fig. 5(b) contains only one peak over frequencies, indicating the two waves have similar wave periods. The segment integration results in Fig. 5(c) verifies this conclusion. Fig. 4(b) illustrates the weather conditions during the experiment. The ship is, therefore, exposed to two short-crested waves with equivalent wave periods of about 6s, and the two waves are both considered wind waves.

The lower energy wave spectrum corresponds to the local wind propagation direction. The experiment was initiated by positioning the vessel towards wind. Considering that the two wave directions are close to 90°, the experiment starts at a ship heading of 0° relative to the wind direction, i.e., lower energy wave component (wave 2), and then rotates until 90°. Correspondingly, the ship heading relative to the stronger wave (wave 1) alters from 90° to 180°. In total, seven cases are recorded in Table 3.

[3] The wave buoy used in this experiment: https://lainepoiss.eu/

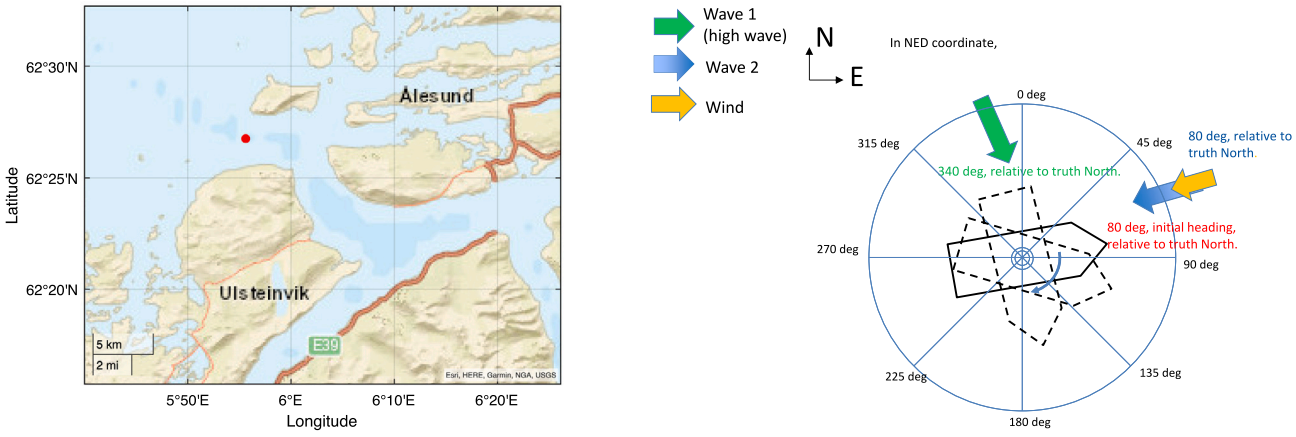

(a) Geographical location. (b) Weather situation

Fig. 4. Field test sites where the vessel was positioned and buoy deployed and surrounding environments.

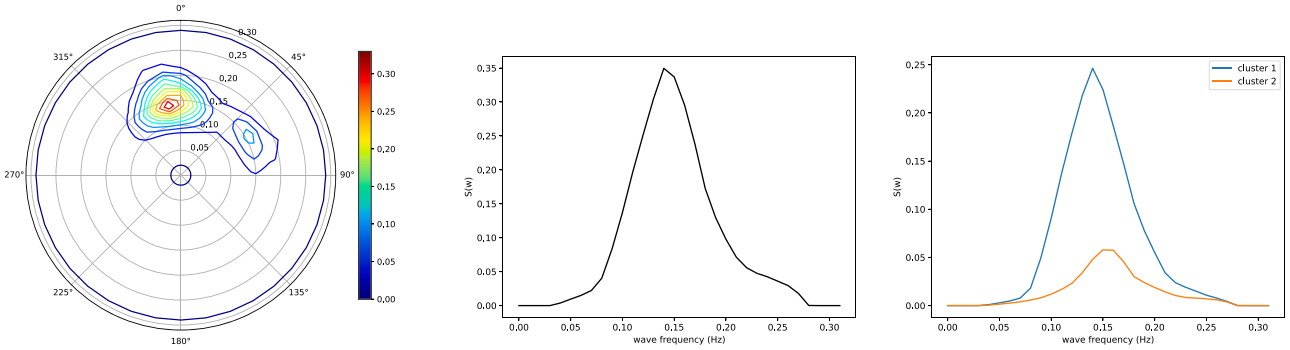

(a) 2D wave spectrum (b) 1D wave spectrum (c) Wave component spectrum

Fig. 5. Radar wave spectrum measurements.

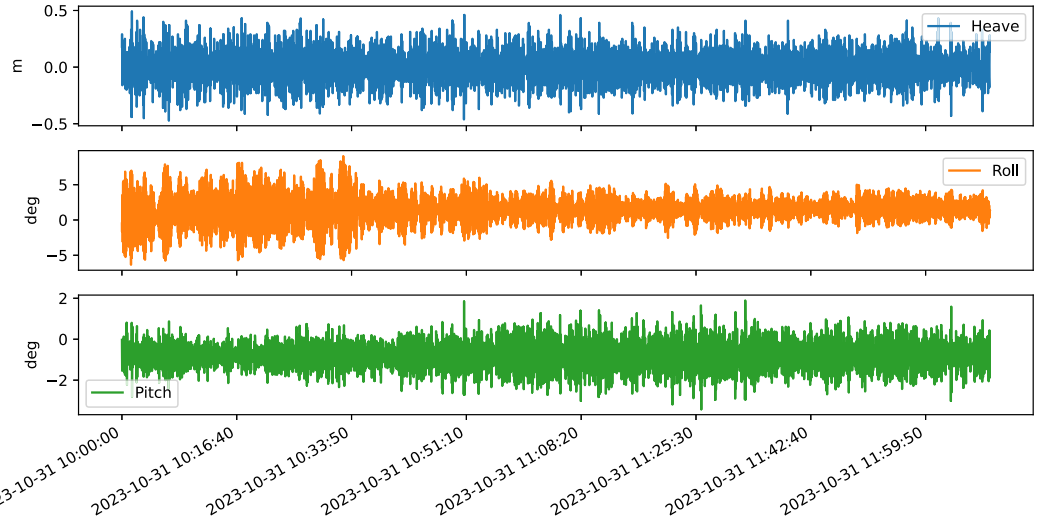

Fig. 6. Time series of vessel responses during the experiment.

3.1. Vessel and crane response

With the sampling frequency of 1 Hz, the ship response in roll, pitch, and heave during the entire experiment are replayed as Fig. 6. As seen, the heave motion remains relatively constant across different ship heading angles, whereas roll and pitch amplitudes vary. Given that the two waves come in directions that are nearly 90° different, when the experiment starts from the head sea to wave 2, the stronger wave 1 comes beam on the ship, causing a higher roll magnitude. The pitch motion consequently shows an opposite trend. Fig. 7 further presents the variations of magnitude and frequency in each DoF motion of the ship. The mean amplitude is represented by standard deviations of

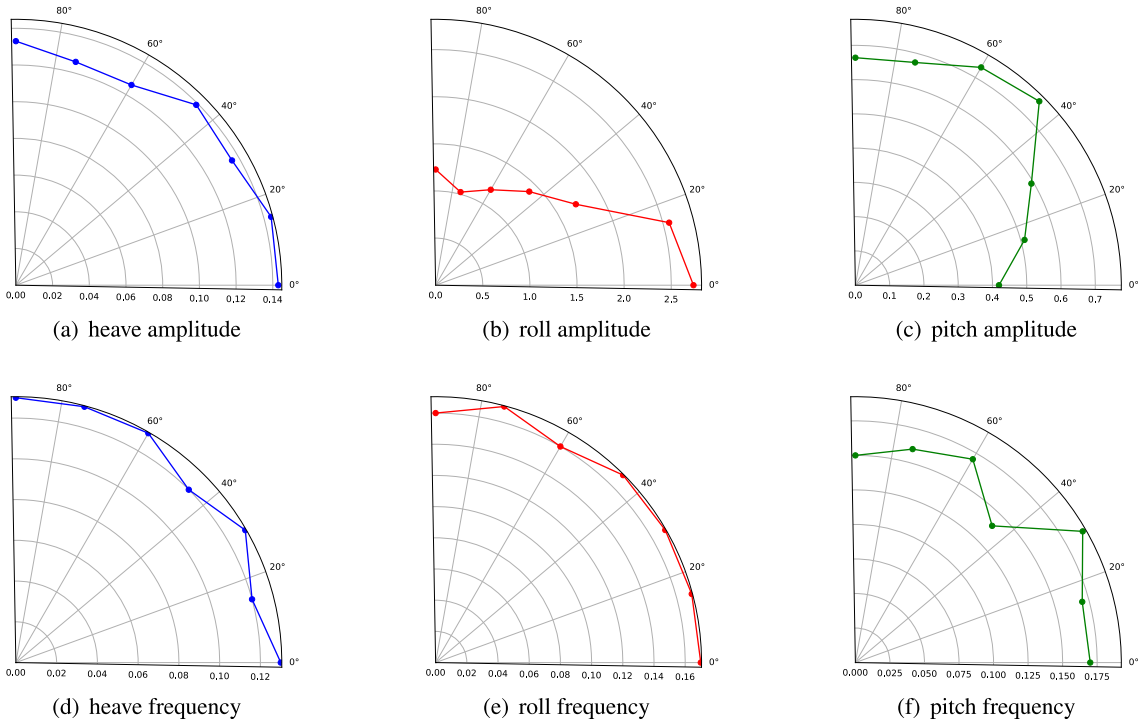

(a) heave amplitude (b) roll amplitude (c) pitch amplitude

(d) heave frequency (e) roll frequency (f) pitch frequency

Fig. 7. Vessel response at each sheltering angle relative to wave 2.

Table 3
Experiment scenarios.

	Angle to wave 1 (main wave direction) (deg)	Angle to wave 2 (deg)
case 1	90 (beam sea)	0 (head sea)
case 2	105	15
case 3	120	30
case 4	135	45
case 5	150	60
case 6	165	75
case 7	180 (following sea)	90 (beam sea)

response, and the peak frequency at each scenario is achieved through fast Fourier transform (FFT). The radius axis in (a) is heave in meters, (b) and (c) are in degrees, and (d)–(f) are in Hz. The polar angles represent the wave attack angle relative to wave 2. The response frequencies of the three DoFs are not affected by wave angles, especially the roll and pitch frequencies, which match the wave frequencies.

The crane vertical motion (in the global frame) is analyzed using forward kinematics, as introduced in Section 2.2. Fig. 8(a) shows a decreasing trend in vertical crane tip movement as the heading angle changes. The crane motion is further analyzed until it is validated against the accelerometer measurements obtained directly from the tip through Figs. 8(b) and 8(c). The accelerations from the sensor are processed through a low-pass filter with a cutoff frequency of 0.3 Hz. A snapshot of FFT analysis in the third case is given in Fig. 9. Screening over all scenarios, the peak frequencies of all scenarios are found to be 0.16 Hz, corresponding to the vessel roll and pitch frequencies.

3.2. Wave elevation in shelter area

The buoy sampled the acceleration with a 50 Hz frequency, and in the field tests, these data were saved in files containing 3,15,000 measurements (circa 105 min). The average is subtracted from the raw measurements to remove any trends and focus on the oscillatory component. The time series of the buoy measurements are presented in Fig. 10. The vertical accelerations are calibrated following the method described in Section 2.3.

Following the data processing procedure, the wave elevations for case 1 are displayed in Fig. 11(a). To validate its accuracy and resolution, the second differentiation of the wave elevation is compared against the measured vertical acceleration. The results of a zoom-in time window are shown in Fig. 11(b), and the two signals are found to match well. Table 4 records the relative errors between the two mean acceleration magnitudes over all scenarios. The results indicate high fidelity in the calculated wave elevations.

3.3. Wave amplitude loss and relative motion

Considering the two objects — crane tip and off-body wave buoy are expected to be located close together during operation to avoid high tension of connecting hawser, the relative movements are analyzed.

As observed in Fig. 8(a), the oscillation magnitude of the crane in the vertical direction decreases with increased relative angle to wave 2. The further response details are presented in Fig. 12(a), where the lower x-axis represents the relative angle to wave 2, and the upper x-axis represents the relative angle to wave 1. As the directional wave spectrum 5(a) indicates, the two wave clusters are distributed at an angle of nearly 90 deg, and the energy of wave 1 is stronger than wave 2. Given such a sea state, the crane movement in Fig. 12(a) is reasonable.

The deviation of wave elevation at the starboard side of the vessel is found in Fig. 12(b). In this figure, case 1 and case 3 are observed to be the best shielding angles, which achieve the lowest wave elevation in the blocked area. 15° to wave 2 and 105° to wave 1 is the scenario with the highest oscillation amplitude. According to hydrodynamics, the response amplitude operation (RAO) of the off-body point decreases from 0° to 90° shelter angle if the single short-crested wave is considered. However, during the field experiment, the vessel was exposed to two short-crested waves with similar wave periods. In the beginning, the shielding of wave 1 leads to a moderate wave elevation on the starboard side; the impact of wave 2 is almost not disturbed by the ship.

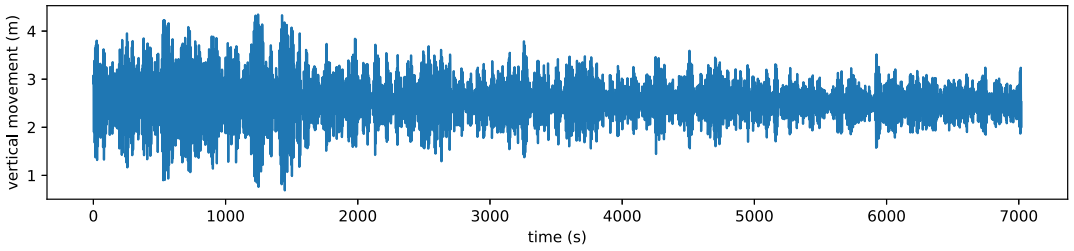

(a) Displacement.

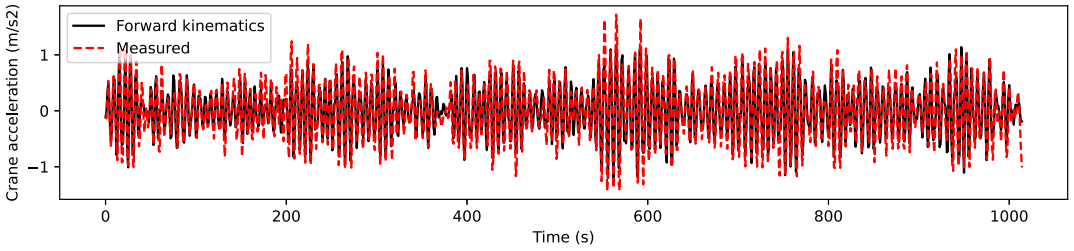

(b) Acceleration.

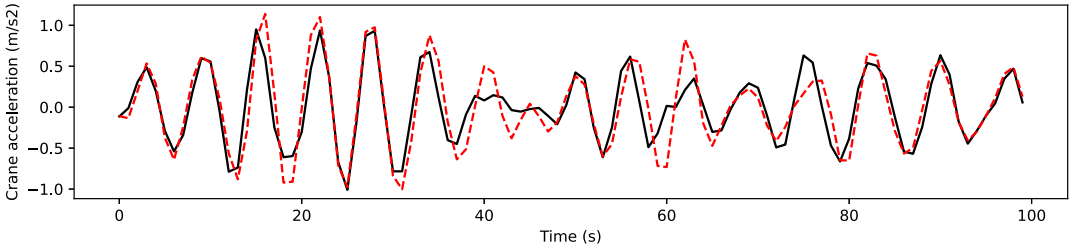

(c) Acceleration zoomed in at 0-100 s

Fig. 8. Crane tip vertical movements in the global frame.

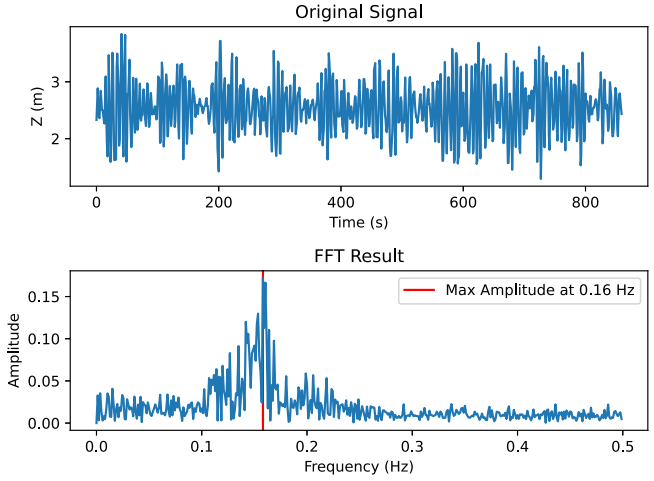

Fig. 9. Crane vertical motion time series and frequency analysis of case 3.

Table 4
Acceleration errors between measured and differentiated values (angles are relative to wave 2).

	0 deg	15 deg	30 deg	45 deg	60 deg	75 deg	90 deg
Measured (m/s^2)	1.554	0.968	0.680	0.551	0.615	0.753	0.717
Differentiated (m/s^2)	1.549	0.966	0.679	0.550	0.614	0.752	0.716
Relative error	0.308%	0.201%	0.187%	0.179%	0.154%	0.141%	0.127%

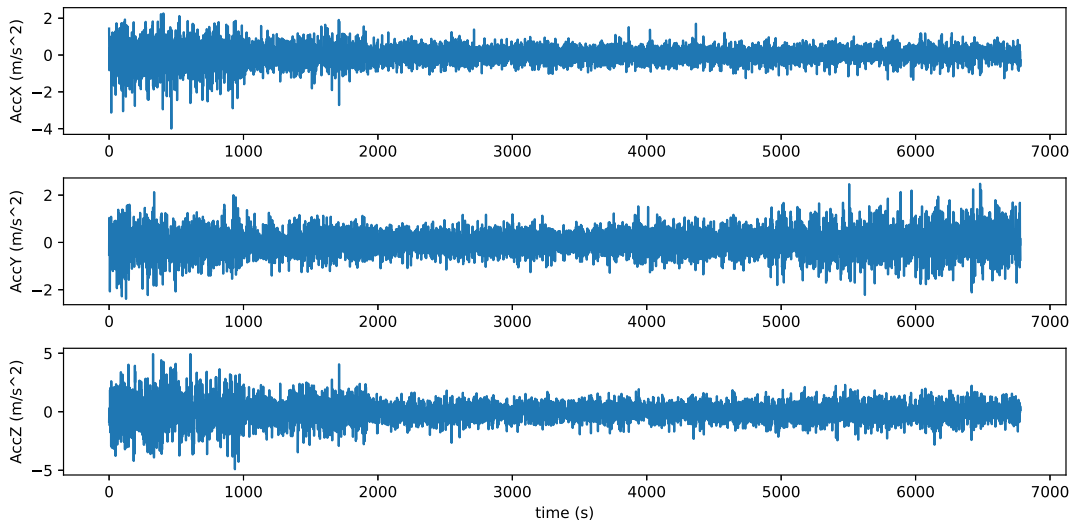

Fig. 10. Wave buoy three-dimensional inertial measurements during experiment.

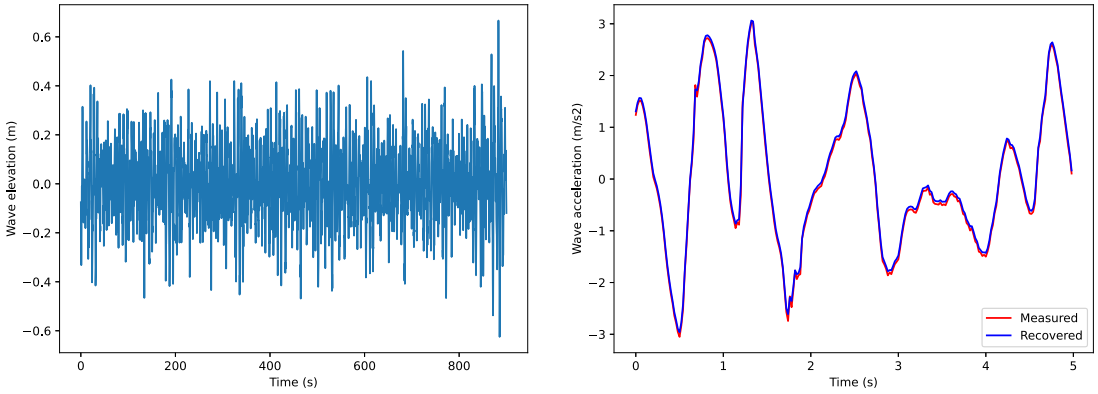

(a) Wave elevation (b) Accelerations

Fig. 11. Wave elevation and acceleration at the sheltered area.

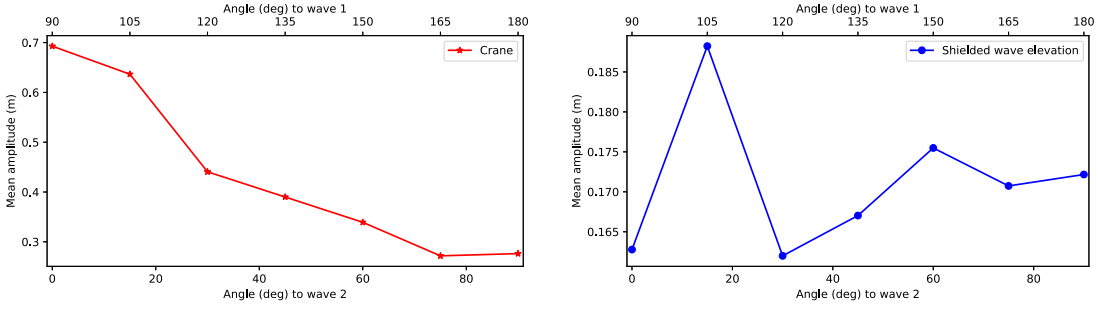

(a) Crane (b) Shielded wave elevation

Fig. 12. Mean amplitudes over relative wave angles from 0° to 90°.

And at the later scenarios, the shielding of wave 2 contributes more. Integrating the two wave components, the wave elevation exhibits such a change. The mean relative motion between the crane tip and the shielded water surface is presented in Fig. 13. The variation is observed to decrease with an increased relative angle to wave 2, which is similar to that of the crane motion.

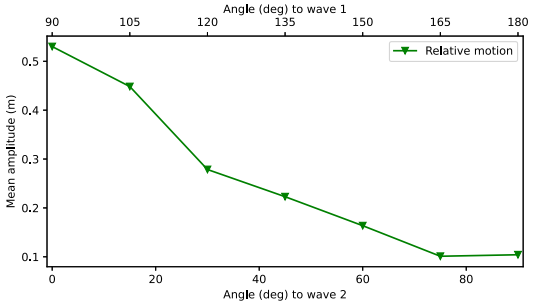

Fig. 13. Mean relative distance between crane tip and the shielded water surface.

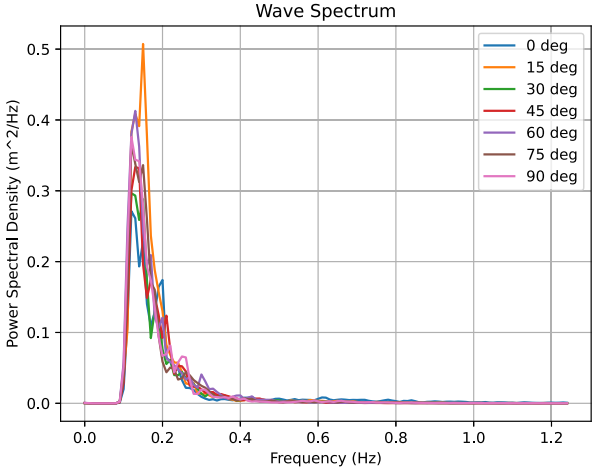

Fig. 14. Shielded wave spectrum derived by wave elevations, where the legends correspond to relative angle with wave 2.

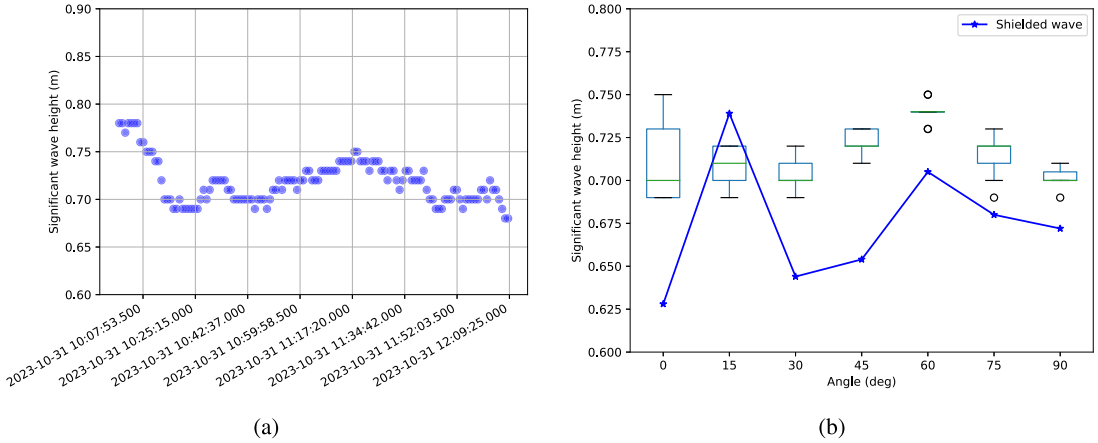

Fig. 15. Significant wave height of incident and shielded waves.

Fig. 14 reveals the shielded wave spectrum. Based on the spectrum, the relevant wave parameters calculated according to (6) are recorded in Table 5. The incident waves measured by the RangeFinder is exhibited in Fig. 15(a). Relating the two wave profiles in Fig. 15(b), a general wave elevation amplitude loss is captured. The largest loss of 11.4% takes place in case 1 (0° to wave 2). Case 3 and case 4 show similar drops of 8.4% and 9.7%, respectively. Case 2, when the ship is positioned 15° to wave 2 and 105° to wave 1, shows slightly stronger waves on the sheltered side than the weather side. This phenomenon does not usually happen and is probably not being sheltered from both

Table 5
Shielded wave field parameters (angles are relative to wave 2).

	0 deg	15 deg	30 deg	45 deg	60 deg	75 deg	90 deg
H_s (m)	0.628	0.739	0.644	0.654	0.705	0.680	0.672

waves or affected by the propulsion force at the stern, and thereby, it is regarded as an outlier.

In this specific experiment, the most effective wave shielding occurs when the vessel is positioned 90° or 120° to wave 1, but the crane will move severely at these headings. Due to the limitation of the ship size, the variance of shielded wave elevations is not as large as that of the crane. Therefore, if the smallest crane movement is pursued, the ship should be positioned [165°, 180°] towards the main wave direction, which also leads to a reasonable, although not best, wave elevation on the downwind side.

4. Discussions

The field experiment highlighted several challenges inherent in real-world marine operations, including device deployment and data collection in the open sea, measurement processing, time-varying weather, etc. Any instrument can introduce a margin of error. Human factors can also introduce inconsistencies when deploying sensors. These factors make the field experiment vulnerable. Meanwhile, multiple short-crested waves in varying directions posed complex challenges that simulations had not anticipated. For example, simulations often simplify ocean conditions, assuming one dominant wave direction, while in reality, vessels are exposed to a mix of wave systems with different periods and directions. This difference between simulated and real-world conditions underscores the importance of conducting full-scale field experiments.

Despite these complexities, the experiment provided valuable insights into wave shielding effects. For example, the significant reduction in crane movement and wave elevation when the vessel was positioned 165 to 180 degrees towards the dominant wave suggests that optimal heading control can increase the operational window in offshore environments. However, limitations remain. The experiment was performed under specific weather conditions on a single day, and additional experiments under different wave systems and environmental factors are necessary to generalize the results. Nonetheless, this study offers a promising step forward in understanding and mitigating wave impacts on marine operations. The findings have practical implications for improving operational stability during lifting operations in challenging marine environments. By optimizing vessel positioning relative to incoming waves, it is possible to minimize crane motion, reduce wave impacts on the sheltered side, and improve overall safety and efficiency in offshore operations.

5. Conclusion

This paper investigated the wave shielding effects through a detailed field experiment, focusing on optimizing vessel positioning to minimize dynamic responses and increase the operational window during offshore crane operations. The results demonstrate that a heading range of 165° to 180° towards the primary wave yields the best overall performance, with reduced crane movement and wave elevation in the sheltered area. Additionally, headings between 90° and 120° were found to provide a relatively calm area, although the crane movements were more pronounced.

These findings offer valuable insights for enhancing safety and efficiency in marine operations by utilizing wave shielding effects and vessel heading control. Future work should focus on expanding the experiments to include a broader range of wave conditions and vessel types, ensuring more generalized conclusions that can be applied to diverse offshore environments.

CRediT authorship contribution statement

Tongtong Wang: Writing – original draft, Methodology, Investigation, Conceptualization. **Robert Skulstad:** Writing – review & editing. **Finn Tore Holmeset:** Investigation. **Karl Henning Halse:** Writing – review & editing. **Hans Petter Hildre:** Project administration. **Houxiang Zhang:** Project administration.

Declaration of competing interest

The authors declare that they have no known competing financial interests or personal relationships that could have appeared to influence the work reported in this paper.

Acknowledgment

This work was supported by a grant from the Research Council of Norway through "The Digital Ocean Space - Møre Ocean Lab" Project 322535.

References

Alari, V., Björkqvist, J.V., Kaldvee, V., Mölder, K., Rikka, S., Kask-Korb, A., Vahter, K., Pärt, S., Vidjajev, N., Tõnisson, H., 2022. LainePoiss®—A lightweight and ice-resistant wave buoy. J. Atmos. Ocean. Technol. 39 (5), 573–594. http://dx.doi.org/10.1175/JTECH-D-21-0091.1.

Chang, C.H., Kontovas, C., Yu, Q., Yang, Z., 2021. Risk assessment of the operations of maritime autonomous surface ships. Reliab. Eng. Syst. Saf. 207 (September 2020), 107324. http://dx.doi.org/10.1016/j.ress.2020.107324.

Chu, Y., Li, G., Hatledal, L.I., Holmeset, F.T., Zhang, H., 2021. Coupling of dynamic reaction forces of a heavy load crane and ship motion responses in waves. Ships Offshore Struct. 16 (S1), 58–67. http://dx.doi.org/10.1080/17445302.2021.1907066.

Cong, P.W., Magee, A.R., Jaiman, R., Ge, S.Z., Zhang, Q., Tu, F.W., Choudhary, A., Merchant, A., Hussain, A., Xu, W., 2018. Hydrodynamic analysis including shielding effects and advanced DP controls for improved uptime of a floatel connected to an FPSO by a gangway. In: Technology Conference Asia 2018. OTCA 2018, http://dx.doi.org/10.4043/28372-ms.

Craig, J.J., 2006. Introduction to Robotics. Pearson Educacion.

Guanche, R., Martini, M., Jurado, A., Losada, I.J., 2016. Walk-to-work accessibility assessment for floating offshore wind turbines. Ocean Eng. 116, 216–225. http://dx.doi.org/10.1016/j.oceaneng.2016.03.013.

Huang, H., Chen, X., Ji, S., Miao, Y., Chen, X., 2023. Experimental and numerical study on dynamic responses of floating bridge under the shielding effect of a floating platform. Mar. Struct. 89 (July 2022), 103379. http://dx.doi.org/10.1016/j.marstruc.2023.103379.

Li, B., 2020. Multi-body hydrodynamic resonance and shielding effect of vessels parallel and nonparallel side-by-side. Ocean Eng. 218 (October), 108188. http://dx.doi.org/10.1016/j.oceaneng.2020.108188.

Li, B., 2021. Operability study of walk-to-work for floating wind turbine and service operation vessel in the time domain. Ocean Eng. 220 (September 2020), 108397. http://dx.doi.org/10.1016/j.oceaneng.2020.108397.

Li, L., Gao, Z., Moan, T., 2015. Comparative study of lifting operations of offshore wind turbine monopile and jacket substructures considering vessel shielding effects. In: Proceedings of the International Offshore and Polar Engineering Conference 2015-Janua, vol. 2015-Janua, pp. 1290–1298.

Li, L., Gao, Z., Moan, T., 2016. Analysis of lifting operation of a monopile considering vessel shielding effects in short-crested waves. Int. J. Offshore Polar Eng. 26 (4), 408–416. http://dx.doi.org/10.17736/ijope.2016.tsr09.

Oh, S., Jung, D.-W., Kim, Y.-H., Kwak, H.-U., Jung, J.-H., Jung, S.-J., Park, B., Cho, S.-K., Jung, D., Sung, H.G., 2020. Numerical study on characteristics and control of heading angle of floating LNG bunkering terminal for improvement of loading and off-loading performance. J. Ocean. Eng. Technol. 34 (2), 77–88. http://dx.doi.org/10.26748/ksoe.2020.007.

Queiroz Filho, A.N., Tannuri, E.A., 2009. DP offloading operation: A numerical evaluation of wave shielding effect. In: IFAC Proceedings Volumes (IFAC-PapersOnline), vol. 42, (no. 18), IFAC, pp. 382–387. http://dx.doi.org/10.3182/20090916-3-BR-3001.0015.

Ren, Z., Verma, A.S., Li, Y., Teuwen, J.J., Jiang, Z., 2021. Offshore wind turbine operations and maintenance: A state-of-the-art review. Renew. Sustain. Energy Rev. 144 (January), http://dx.doi.org/10.1016/j.rser.2021.110886.

Semedo, A., Vettor, R., Breivik, Sterl, A., Reistad, M., Soares, C.G., Lima, D., 2015. The wind sea and swell waves climate in the Nordic seas. Ocean Dyn. 65 (2), 223–240. http://dx.doi.org/10.1007/s10236-014-0788-4.

Wang, T., Li, G., Hatledal, L.I., Skulstad, R., Aesoy, V., Zhang, H., 2022. Incorporating approximate dynamics into data-driven calibrator: A representative model for ship maneuvering prediction. IEEE Trans. Ind. Inform. 18 (3), 1781–1789. http://dx.doi.org/10.1109/TII.2021.3088404.

Wang, T., Li, G., Wu, B., Æsøy, V., Zhang, H., 2021. Parameter identification of ship manoeuvring model under disturbance using support vector machine method. Ships Offshore Struct. 16 (S1), 13–21. http://dx.doi.org/10.1080/17445302.2021.1927600.

Zhang, H., Li, G., Hatledal, L.I., Chu, Y., Ellefsen, A., Han, P., Major, P., Skulstad, R., Wang, T., Hildre, H.P., 2023. A digital twin of the research vessel gunnerus for lifecycle services: Outlining key technologies. IEEE Robot. Autom. Mag. 30 (3), 6–19. http://dx.doi.org/10.1109/MRA.2022.3217745.

Zhao, W., Pan, Z., Lin, F., Li, B., Taylor, P.H., Efthymiou, M., 2018. Estimation of gap resonance relevant to side-by-side offloading. Ocean Eng. 153 (January), 1–9. http://dx.doi.org/10.1016/j.oceaneng.2018.01.056.